Atomic Insights into Aluminium-Ion Insertion in Defective Anatase for Batteries

Christophe Legein, Benjamin Morgan, Franck Fayon, Toshinari Koketsu, Jiwei Ma, Monique Body, Vincent Sarou-kanian, Xian-kui Wei, Marc Heggen, Olaf Borkiewicz, et al.

Atomic Insights into Aluminium-Ion Insertion in Defective Anatase for Batteries

Christophe Legein[a], Benjamin J. Morgan[b], Franck Fayon[c], Toshinari Koketsu[d], Jiwei Ma[e],[g], Monique Body[a], Vincent Sarou-Kanian[c], Xian-Kui Wei[f], Marc Heggen[f], Olaf J. Borkiewicz[i], Peter Strasser[d], and Damien Dambournet[e],[f]*

[a] Prof. C. Legein, Dr. M. Body
Institut des Molécules et des Matériaux du Mans (IMMM), UMR 6283 CNRS, Le Mans Université,
Avenue Olivier Messiaen, 72085 Le Mans Cedex 9, France
[b] Dr. B. J. Morgan
Department of Chemistry
University of Bath
BA2 7AY Bath, United Kingdom
[c] Dr. F. Fayon, Dr. V. Sarou-Kanian
CNRS, CEMHTI UPR3079
Université d'Orléans
F-45071 Orléans, France
[d] Dr. T. Koketsu, Prof. P. Strasser
The Electrochemical Energy, Catalysis, and Materials Science Laboratory, Department of Chemistry
Technical University Berlin
10623 Berlin, Germany
[e] Pr. J. Ma, Dr. D. Dambournet
Sorbonne Université, CNRS,
Physico-chimie des électrolytes et nano-systèmes interfaciaux, PHENIX,
F-75005 Paris, France
E-mail: damien.dambournet@sorbonne-universite.fr
[f] Dr. D. Dambournet
Réseau sur le Stockage Electrochimique de l'Energie (RS2E)
FR CNRS 3459
80039 Amiens cedex, France
[g] Pr. J. Ma
Institute of New Energy for Vehicles,
School of Materials Science and Engineering, Tongji University,
Shanghai 201804, China
[h] Dr. X. Wei, Dr. M. Heggen
Forschungszentrum Juelich GmbH
52425 Juelich, Germany
[i] Dr. O. J. Borkiewicz
X-ray Science Division, Advanced Photon Source
Argonne National Laboratory
9700 South Cass Avenue, Argonne, Illinois 60439, United States

Supporting information for this article is given via a link at the end of the document.((Please delete this text if not appropriate))

Abstract: Aluminium batteries constitute a safe and sustainable high–energy-density electrochemical energy-storage solution. Viable Al-ion batteries require suitable electrode materials that can readily intercalate high-charge Al^{3+} ions. Here, we investigate the Al^{3+} intercalation chemistry of anatase TiO_2 and how chemical modifications influence the accommodation of Al^{3+} ions. We use fluoride- and hydroxide-doping to generate high concentrations of titanium vacancies. The coexistence of these hetero-anions and titanium vacancies leads to a complex insertion mechanism, attributed to three distinct types of host sites: native interstitials sites, single vacancy sites, and paired vacancy sites. We demonstrate that Al^{3+} induces a strong local distortion within the modified TiO_2 structure, which affects the insertion properties of the neighbouring host sites. Overall, specific structural features induced by the intercalation of highly-polarizing Al^{3+} ions should be considered when designing new electrode materials for polyvalent batteries.

Introduction

Lithium-ion batteries are used for electrochemical storage in multiple applications, ranging from electronic devices to electric vehicles and to grid storage. The continuing growth in global energy demands calls for the development of new energy storage technologies with increased efficiencies, decreased environmental impact, and higher energy densities. Concerns about whether lithium resources can meet projected future energy-storage needs has motivated research into alternative ion-insertion electrochemistries.[1–4] One possible alternative to lithium-ion batteries is to exploit aluminium-ion intercalation chemistries. Aluminium-ion batteries would take advantage of the greater abundance of aluminium compared to lithium, and they offer the potential for increased energy densities and improved battery safety.[5] Aluminium is the third most abundant element, and the most abundant metal, in the Earth's crust, making it significantly cheaper than lithium.[6] Furthermore,

aluminium can exchange up to three electrons per ion, versus one electron per ion for lithium, and has a high density (2.7 g cm^{-3} at 25 °C). This gives a high theoretical volumetric capacity of 8056 mAh cm^{-3} for aluminium, versus 2042 mAh cm^{-3} for lithium.[7]

A key challenge in developing aluminium-ion batteries is identifying suitable electrode materials, that can reversibly intercalate Al^{3+} ions.[8] The ionic radius of the Al^{3+} ion (0.53 Å) is smaller than that of Li^+ (0.76 Å), and one might therefore expect to find many materials that readily intercalate Al^{3+} insertion. In practice, strong interactions between high formal-charge Al^{3+} and the anionic substructure of the host material mean insertion is often severely limited. The polarizing power of an ion is given by Z/r^2, where Z and r are its charge and its radius, respectively. The polarizing power describes the degree to which a given cation attracts and distorts the electron clouds of nearby anions. The polarizing power of Al^{3+} (10.68 e $Å^{-2}$) is much greater than that of Li^+ (1.73 e $Å^{-2}$), consistent with a stronger electrostatic interaction between Al^{3+} and the anionic sublattice of an intercalation host. This stronger interaction means that, in general, the intercalation behaviour of polyvalent cations often strongly differs from that of lithium ions.[4]

Because few materials are known that readily accommodate Al^{3+} ions, there is a limited understanding of Al^{3+} intercalation chemistry. Efficient aluminium storage has been reported for graphite cathode materials, but this relies on *anionic* intercalation of $AlCl_4^-$ species, as opposed to intercalation of trivalent Al^{3+}.[9] Other organic compounds have also been found to be electrochemically active, again through anionic intercalation.[10] Because of the difficulty in identifying suitable Al^{3+}-host materials, a limited number of studies have explored Al^{3+}-intercalation in inorganic frameworks.[5,11–19] One strategy for identifying new Al-cathode materials is to first build a detailed understanding of the intercalation (electro)chemistry of known, viable Al-intercalation hosts; in particular, seeking to understand the local chemical environment of inserted Al in these materials, and how this affects electrochemical performance.

Anatase TiO_2 consists of a three-dimensional network of corner- and edge-sharing TiO_6 octahedra, with interstitial sites that can readily accommodate lithium and sodium ions.[20,21] We have previously shown that anatase TiO_2 can be chemically modified through monovalent-ion (F^-, OH^-) doping, producing cation vacancies that allow reversible intercalation of polyvalent Mg^{2+} and Al^{3+} cations.[22] The insertion behaviours of these two cations are qualitatively different: while Mg can fully occupy all available titanium vacancies, Al^{3+} cations occupy barely half of the available sites. In the study presented herein, we further investigate the Al^{3+} intercalation mechanism in cation-deficient anatase TiO_2, to resolve specific details of Al^{3+} intercalation chemistry in this model host electrode material. Our results indicate a complex insertion mechanism involving a variety of insertion sites: isolated single-vacancy sites, adjacent-pair double-vacancy sites, and native interstitial sites. The identities of the surrounding anions at specific insertion sites and the polarizing power of Al^{3+} ions are highlighted as key factors that impact the total number of inserted ions.

Results and Discussion

Figure 1a shows a typical galvanostatic first discharge/charge curves[23] for an anatase electrode with ~22% Ti vacancies ($Ti_{0.78}□_{0.22}O_{1.12}F_{0.40}(OH)_{0.48}$)[24]. The discharge and charge capacities correspond to the insertion of ~0.103 (117 mAh g^{-1}) and ~0.080 Al^{3+} (92 mAh g^{-1}) per formula unit, respectively. These values are three-times higher than measured for defect-free TiO_2.[18,22] To confirm the electrochemical insertion of Al^{3+} ions into the structure, high-angle annular dark-field (HAADF) imaging with a scanning transmission electron microscope (STEM) coupled with energy-dispersive X-ray (EDX) spectroscopy was performed on the discharged electrode **(Figure1b,c)**. The resulting data show that aluminium insertion extends throughout the particle giving a homogenous distribution of Al at the nanometer scale. Quantitative analysis obtained by EDX indicates an Al/Ti molar ratio of 0.13. Considering a three-electron transfer per inserted ion, this number matches the experimental capacity, further supporting the insertion of Al^{3+}.

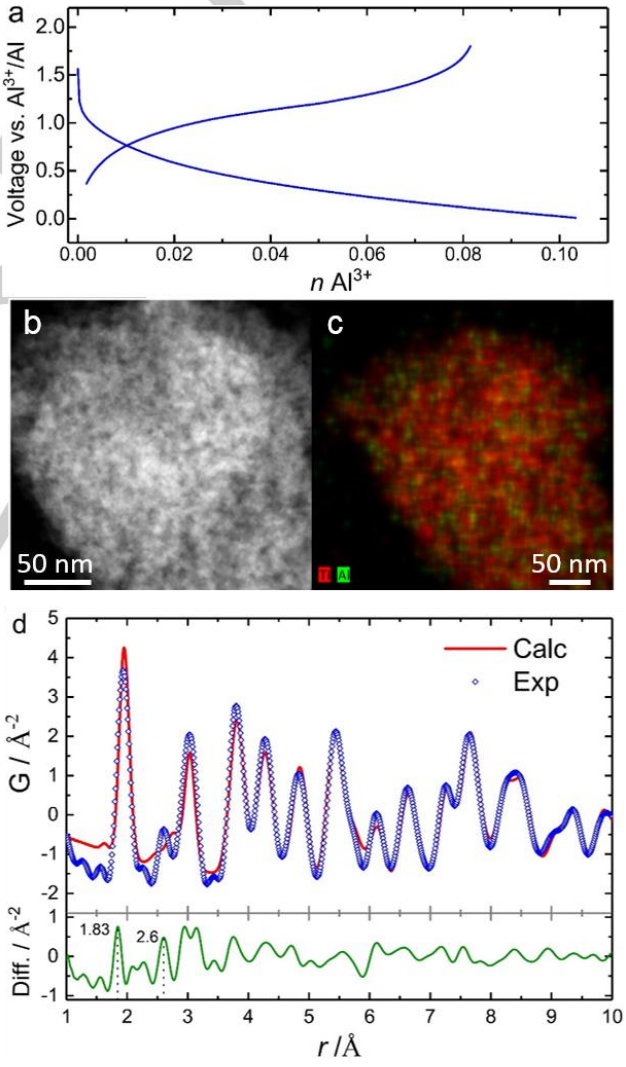

Figure 1. (a) Galvanostatic first discharge and charges curves obtained for $Ti_{0.78}□_{0.22}O_{1.12}F_{0.40}(OH)_{0.48}$ electrode cycled vs. Al^{3+}/Al under 20 mA g^{-1} at 25 °C. **(b,c)** HAADF-STEM image measured on the discharged electrode and the corresponding EDX mapping acquired at the K edge of Al (green) and Ti (red) elements overlaid in the image. The measured atomic percentages (at%) are 88.5 at% for Ti and 11.5 at% for Al. **(d)** PDF refinement obtained on the discharged electrode. Green line, difference curve between calculated and experimental data.

The continuous decrease of the voltage-composition curve is typical of solid-solution behaviour. To confirm such a mechanism, the atomic structure of a discharged electrode was analysed. We used the pair distribution function (PDF) obtained by Fourier Transform of the correlation function[25] to capture any local structural changes induced by Al^{3+} intercalation. The PDF represents the probability of finding a pair of atoms separated by a distance *r* (inter-atomic distances), and describes atomic ordering over short-to-intermediate distances.[26] Using stoichiometric anatase TiO_2 as structural model, the PDF data were successfully refined, with particularly good agreement for interatomic distances greater than 4 Å (**Figure 1d and Figures S1 & S2** in the Supporting Information), confirming that the parent anatase framework is maintained upon Al intercalation. The unit cell parameters remained almost unchanged with *a* = 3.7972(7) Å and *c* = 9.478(3) Å for stoichiometric anatase, and *a* = 3.802(1) Å

and *c* = 9.479(6) Å for the discharged electrode. Negligible volume changes upon Al^{3+} intercalation have been reported previously for other materials.[14,16,17,27] The PDF data for *r* < 4 Å describes the local structure, and in this regime we find large deviations from the calculated stoichiometric anatase data. The difference curve highlights interatomic distances at ~1.83 Å and ~2.6 Å that are not captured by the anatase model. These features are less pronounced after charging (See Supporting Information) suggesting that they are induced by the intercalation of Al^{3+}. The residual peak observed at around 1.83 Å can be tentatively assigned to Al-*X* (*X* = F/OH[28–31],O[32]) while the sharp peak observed at 2.6 Å is attributed to F-F(OH)[28–31] and short O-O(OH) distances. Finally, we attempted to localize Al^{3+} ions within the structure by refining its occupancy in the titanium vacancies and the native interstitial sites. This refinement gives 0.11(3) Al^{3+} within the titanium vacancies and 0.02(2) Al^{3+} in the interstitial sites. Within the uncertainty of these data, these values agree with the measured insertion capacity, and suggest that inserted Al^{3+} ions preferentially occupy titanium vacancy sites.

Owing to its sensitivity to the local atomic-scale structure, high magnetic-field (20 T) solid-state ^{27}Al MAS NMR was used to probe the intercalation environments of the aluminium atoms (**Figure 2**). The one-dimensional ^{27}Al MAS NMR spectrum of the central transitions of the discharged electrode was reconstructed using two groups of resonances arising from inserted Al^{3+} ions and impurities, respectively (**Figure S3** and **Table S1**). The latter group includes two contributions with a narrow dissymmetric peak at ~101 ppm, assigned to $AlCl_4^-$ and $Al_2Cl_7^-$[33] coming from unwashed electrolyte, and a weaker intensity peak at 82 ppm, tentatively assigned to $Al(OH)_4^-$.[34]

The main resonances, assigned to inserted Al^{3+} ions, consist of three overlapping broad lines with isotropic chemical shifts (δ_{iso}) assigned to tetra-, penta-, and hexa-coordinated aluminium ($^{[n]}$Al with *n* = 4, 5, or 6). The line shapes are characteristic of disordered $^{[n]}$Al sites and their reconstruction was achieved considering Gaussian distributions of δ_{iso} and C_Q (nuclear quadrupole coupling constant) values.[35] $^{[4]}$Al, $^{[5]}$Al and $^{[6]}$Al resonances feature large isotropic chemical shift distributions (**Figure 2a**, **Table S1**) highlighting strong local disorder. This suggests that Al-intercalation sites exhibit a broad range of local anionic environments, including large radial and angular distortions, which we ascribe to substitutional disorder at both the titanium site (mixed occupancy by Ti^{4+}, Ti^{3+}, Al^{3+} and vacancies) and the anionic site (mixed occupancy by O^{2-}, OH^-, and F^-), and possible additional Al^{3+} ion occupation of interstitial sites.

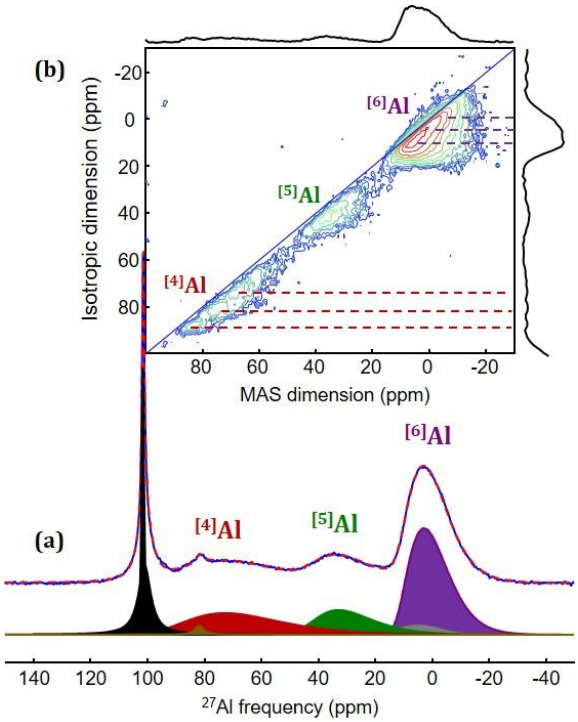

Figure 2. (a) Experimental (blue) and fitted (red dashed) one-dimensional ^{27}Al MAS (60 kHz) NMR (20 T) spectrum of the central transitions of the aluminized $Ti_{0.78}\square_{0.22}O_{1.12}F_{0.40}(OH)_{0.48}$ sample. Details about the fit are given as Supporting Information (**Figure S3**, **Table S1)**. The six central-contributions and the center band of $^{[6]}$Al external transition pattern (in grey) are shown below. **(b)** Two-dimensional ^{27}Al 3QMAS spectrum of this sample. 4-, 5- and 6-fold coordinated aluminium resonances are indicated. The dashed lines indicate the δ_{iso} values of the suggested overlapping contributions within the broad lines assigned to $^{[4]}$Al and $^{[6]}$Al sites.

The relative intensities of the $^{[n]}$Al resonances indicate the preferential formation of $^{[6]}$Al (55 %), versus $^{[5]}$Al (18 %), and $^{[4]}$Al (27 %). To improve the spectral resolution of these $^{[n]}$Al sites, a ^{27}Al 3QMAS spectrum was recorded (**Figure 2b**) highlighting a $^{[6]}$Al resonance with a complex line shape, due to a large isotropic chemical shift distribution, correlated to a distribution of quadrupolar parameters. The asymmetric line-shape in the isotropic dimension suggests several overlapping contributions with δ_{iso} values of about 10 ppm, 5 ppm, and 0 ppm **(see dashed lines in Figure 2b)**. These values are characteristic of $AlO_{6-x}F_x$[36,37] and $Al(OH)_{6-x}F_x$[31] environments, with $x \leq 2$, in aluminium oxy- and hydroxy-fluorides (in general, the higher the fluorine content, the lower the chemical shift). Due to the preferential location of F atoms in the vicinity of titanium vacancies,[24] the average *x* value of the environment of the vacancies ($\square(O,OH)_{6-x}F_x$), and therefore of the Al atoms inserted in these sites, is *x* = 2.32.[38] The difference in the degree of fluorination (*x*) is related to the presence of other cations (Ti^{4+}, Ti^{3+}), that affect the chemical shift values with respect to the above mentioned reference samples. The ^{27}Al 3QMAS spectrum also reveals large isotropic chemical-shift distributions for the $^{[4]}$Al and $^{[5]}$Al sites, as indicated by the spread along the diagonal of the 2D map. Three $^{[4]}$Al contributions (at ~88 ppm, ~78 ppm,

and ~70 ppm) appear just above the noise level; which are assigned to $Al(O,OH)_4$ units with O(OH) atoms bridging Al and 1 or 2 Ti (Ti^{III} or Ti^{IV}) atoms. We note that different coordination modes can be found in crystalline transition aluminas, which exhibit $^{[4]}Al$ and $^{[6]}Al$ sites, and that $^{[4]}Al$ and $^{[5]}Al$ sites are dominant in amorphous aluminium oxides.[39–41]

Complementary insights about the aluminium insertion mechanism were obtained from ^{19}F solid-state NMR. ^{19}F NMR is a suitable probe for Al^{3+} insertion in titanium vacancies because the ^{19}F chemical shift strongly depends on the number and nature of the fluorine–nearest-neighbours. **Figure 3a** shows the ^{19}F MAS NMR (7 T) spectrum of the pristine $Ti_{0.78}\square_{0.22}O_{1.12}F_{0.40}(OH)_{0.48}$. The fluorine environments $Ti^{IV}\square_2$–F, $Ti^{IV}{}_2\square$–F, and $Ti^{IV}{}_3$–F were previously identified at δ_{iso} values of about 98 ppm, -4 ppm, and -88 ppm, respectively.[22,24] To allow direct comparison and to avoid isotropic lines and spinning sidebands overlapping, ^{19}F NMR spectra of the discharged electrode were also recorded at moderate field (**Figure 3b**).

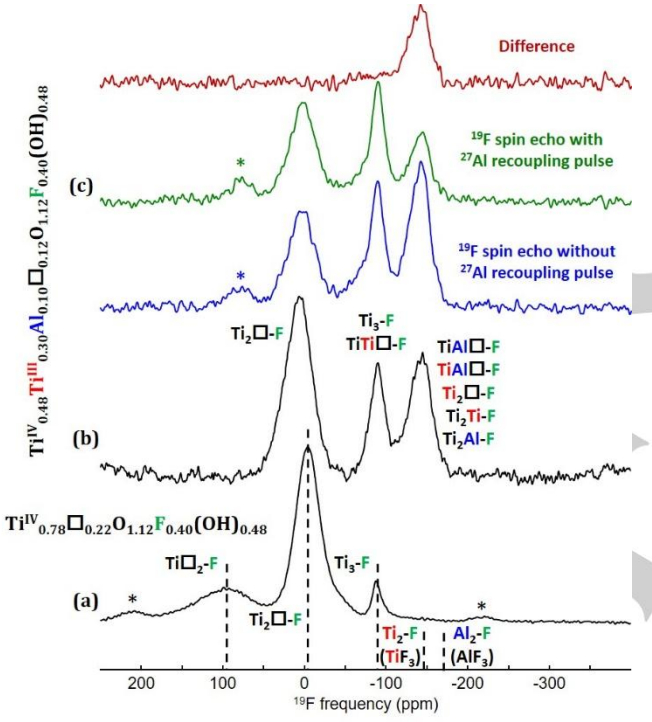

Figure 3. ^{19}F MAS NMR (7 T) spectra of **(a)** $Ti_{0.78}\square_{0.22}O_{1.12}F_{0.40}(OH)_{0.48}$ (60 kHz)[22,24] and **(b)** the aluminized sample (64 kHz). **(a)** The asterisks indicate the main spinning sidebands. The dashed lines indicate the ^{19}F δ_{iso} values of $Ti^{IV}{}_3$–F, $Ti^{IV}{}_2\square$–F, and $Ti^{IV}\square_2$–F environments in $Ti_{0.78}\square_{0.22}O_{1.12}F_{0.40}(OH)_{0.48}$ and the ^{19}F δ_{iso} values of $Ti^{III}{}_2$–F environment in TiF_3 and Al_2–F environment in AlF_3. **(b)** Fit of the spectrum of the aluminized sample is given as Supporting Information (**Figure S4**, **Table S2**). Tentative assignment of the NMR resonances to various species in the aluminized sample are indicated with Ti^{IV} in black and Ti^{III} in red (**Figure S5**). **(c)** ^{19}F-^{27}Al double resonance MAS (60 kHz) NMR (20 T) experiments on the aluminized sample: difference (in red) between the ^{19}F spin echo spectra without ^{27}Al irradiation (in blue) and with ^{27}Al irradiation (in green).

Our data show that aluminium insertion induces the disappearance of the line at ~100 ppm, which is characteristic of $Ti^{IV}\square_2$-F species, providing additional evidence for the preferential insertion of aluminium at these titanium vacancies. We also observe large changes in the relative resonance intensities and moderate changes of the δ_{iso} values of the two other resonances, as well as the appearance of a new resonance at ~-143 ppm (**Figure S4** and **Table S2**). Finally, the main resonance at 0 ppm characteristic of $Ti^{IV}{}_2\square$-F slightly shifts to higher δ_{iso} value, with a decrease of the relative intensity of about 20 % **(Figure 3b)**. Such a change can be due to the insertion of Al^{3+} into these single vacancies and/or due to the presence of reduced Ti^{III} that can induce a resonance shift as discussed below.

To assign the ^{19}F NMR resonances, we identified the numerous possible environments around fluorine atoms in the reduced sample and discussed their probability of occurrence. A random distribution of the fluoride ions on the anionic sites would give three-fold coordinate fluorine atoms as most probable. However, (i) as expected from crystal chemistry and demonstrated by ^{19}F solid-state NMR, fluoride ions are preferentially located close to vacancies in the pristine compound[24] *i.e.*, are unlikely to be threefold coordinated, (ii) the reduced sample remains defective, and (iii) fluoride ions are two-fold coordinated in TiF_3[42] and in the various phases of AlF_3[29,43,44] **(see Supporting Information)**. The intercalation of Al^{3+} ion in a titanium vacancy and the reduction of a Ti^{4+} ion into a Ti^{3+} ion are both expected to induce a decrease of the δ_{iso} value of the neighbouring ^{19}F nucleus. Indeed, we first recall that an increase of the fluorine coordination leads to a decrease of the ^{19}F chemical shift value as shown for ^{19}F NMR chemical shift values of the environments $Ti^{IV}\square_2$–F, $Ti^{IV}{}_2\square$–F and $Ti^{IV}{}_3$–F in $Ti_{0.78}\square_{0.22}O_{1.12}F_{0.40}(OH)_{0.48}$.[24] Moreover, typical ^{19}F NMR chemical shift values found in various AlF_3 phases[45] are ~ - 172 ppm (Al_2–F species). For ^{19}F nucleus close to Ti^{III} as found in TiF_3, it is about -145 ppm ($Ti^{III}{}_2$–F species).[22] Based on these trends and on ^{19}F δ_{iso} values of the F environments in $Ti_{0.78}\square_{0.22}O_{1.12}F_{0.40}(OH)_{0.48}$, we tentatively assign the ^{19}F NMR resonances to some of the potential species expected in the aluminized sample (**Figures 3 and S5, Tables S2 and S6** and more details in the Supporting Information).

^{19}F–^{27}Al double-resonance MAS NMR experiments using a PM-RESPDOR scheme[46] (**Figure 3c**) were performed to explore differences in the ^{19}F-^{27}Al spin-spin and/or residual dipolar couplings, and thus the F-Al connectivities of the different fluorine sites. In the difference spectrum, the ^{19}F resonances at ~ 5 ppm and -90 ppm disappeared, confirming that the corresponding F atoms are not connected to Al atoms, while the ^{19}F resonance at ~ -143 ppm was observed with a relative dephased intensity of 52%. Considering that a subset of ^{27}Al transitions might not be saturated by the ^{27}Al irradiation[46] and that longer dephasing time could be required, this suggests that most of the corresponding F atoms are connected to Al. This supports the tentative assignment of these resonance to $Ti^{IV}{}_2Al$–F, $Ti^{III}Al\square$–F and $Ti^{IV}Al\square$–F species, without excluding a possible contribution of $Ti^{IV}{}_2Ti^{II}$–F, $Ti^{III}{}_2\square$–F species to this peak.

A time-dependent ^{27}Al and ^{19}F solid state NMR study has revealed subtle changes in the different environments of the probed nuclei (see Figures **S6-S10, Tables S3-S6** and discussion in SI). We have observed that Al^{3+} progressively moved from non-fluorinated $^{[4]}Al$ and $^{[5]}Al$ sites to $^{[6]}Al$ sites with the concomitant filling of some $Ti^{IV}{}_2\square$–F vacancies giving $Ti^{IV}{}_2Al$–F species and fluorinated $^{[6]}Al$ site. We concluded that these changes associated with Al^{3+} migration were probably induced by frictional local heating during the NMR experiments. This point requires further investigation.

To better understand the insertion of Al into cation-deficient anatase TiO_2, we performed a series of density functional theory

(DFT) calculations to examine (i) the preferential insertion of Al^{3+} into one of the two available sites in paired–titanium-vacancy configurations; and (ii) the effect of local anion environment on the insertion mechanism at single-vacancy and interstitial sites.

To understand the preference for single Al^{3+} insertion within paired-titanium-vacancies, we performed calculations on a $Ti_{126}\square_2O_{248}F_8$ cell, and modelled the successive insertion of two Al^{3+} ions. The structural evolution of the supercell $Ti_{126}\square_1O_{248}F_8$ before and after the intercalation of one Al^{3+} is shown in **Figure 4**. For clarity, we show the double vacancy region and have labelled F sites as (A) to indicate bridging F-species $Ti_2\square$-F and as (B) to indicate terminal F in $Ti\square_2$-F **(Figure 4a)**. For the first Al^{3+} insertion, we predict an intercalation energy of -3.8 eV, which can be compared to the intercalation energy into an interstitial site of stoichiometric anatase TiO_2 of -1.2 eV **(Figure 5(a))** and shows the strong enhancement in the thermodynamic driving force for Al^{3+} insertion due to the presence of vacant cation sites. In this site, Al^{3+} is 6-fold coordinated with an average bond length of 1.84 Å. Similar bond lengths were identified in the PDF data, and were shown to deviate from an ideal anatase structural model. This observation highlights the strong local distortion induced by the insertion of Al^{3+}. To further illustrate this point, we can compare *M*–*X* bond lengths and MX_6 coordination-polyhedron for $M = Li^+$ versus $M = Al^{3+}$. We observe average bond distances of 2.02 Å (Li^+) versus 1.84 Å (Al^{3+}) and 10.3 $Å^3$ (Li^+) versus 8.1 $Å^3$ (Al^{3+}), again highlighting the strong polarizing power of Al^{3+}.

For insertion of a subsequent second Al^{3+} ion into a paired-titanium-vacancy, we predict an intercalation energy of only -2.4 eV. While this is still more thermodynamically favourable than intercalation into stoichiometric anatase TiO_2, it is less favourable than if each aluminium ion were to singly occupy a different paired-vacancy site. The difference in intercalation energy for the first versus second inserted Al^{3+} can be explained by two factors. Insertion of the first Al^{3+} produces a strong contraction of the anion positions around the insertion site, and an associated expansion at the adjacent paired site. As discussed above, this is due to the strong polarizing power of Al^{3+}, with short Al–(O/F) distances indicating strong favourable Coulombic interactions between the inserted Al^{3+} and the host structure. Insertion of a second Al^{3+} causes the anion positions around the second site to contract somewhat, albeit less than for the first Al^{3+} insertion, and at the cost of expanding the coordination octahedron around the first Al^{3+}. Now, both Al^{3+} have longer neighbouring Al–(O/F) distances, indicating a less favourable Coulombic interaction between the intercalated ions and the host structure, than in the singly inserted case (Supporting Information). In addition, double-Al intercalation can form unfavourable F coordination environments, possibly further disfavouring the second Al^{3+} insertion relative to the first. Upon intercalation of one Al^{3+} in one of the double vacancy sites, the bridging F-species $Ti_2\square$–F (A) become three-fold coordinated, yielding Ti_2Al–F species (labelled C), and the terminal fluorine atom in $Ti\square_2$–F (C) becomes two-fold coordinated to one Al and one Ti, yielding $Ti_1Al_1\square$–F species (labelled D). Based on the above-mentioned tentative assignments of the ^{19}F resonances, we note that the species (B) and (C) can then be attributed to $Ti^{IV}{}_2Al$-F and $Ti^{III}Al\square$-F/$Ti^{IV}Al\square$-F species, respectively.

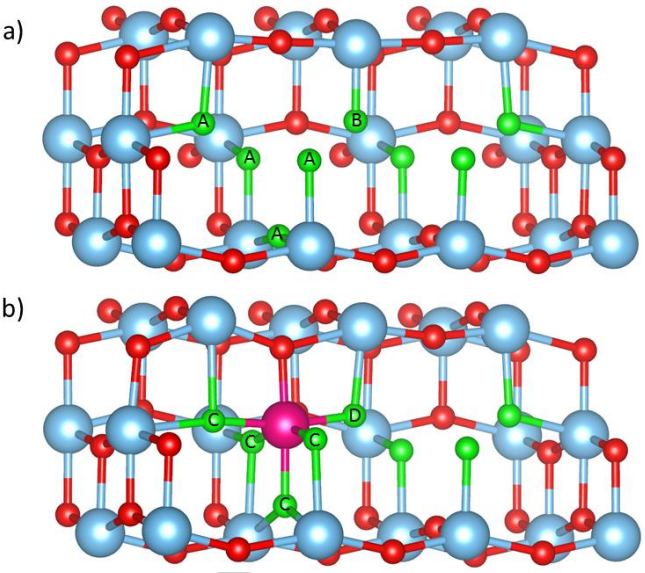

Figure 4. Structural representations of the supercell featuring double vacancy $Ti_{126}\square_2O_{248}F_8$ before a) and after b) the introduction of one Al^{3+}, *i.e.*, $Ti_{126}\square_1Al_1O_{248}F_8$. The blue, red, green and magenta spheres represent titanium, oxygen, fluorine and aluminum atoms, respectively. Labels A-D refer to (A) bridging F-species $Ti_2\square$-F, (B) terminal F in $Ti\square_2$-F, (C) F-species in Ti_2Al-F and (D) F-species in $TiAl\square$-F.

We have also investigated how varying the local anion environment at single-Ti vacancy sites affects the Al^{3+} insertion energies. **Figure 5b** shows calculated intercalation energies for Al^{3+} into $Ti_{127}\square_1O_{252}X_4$ single-vacancy supercells, with the type of single-valent anions (*X*) neighbouring the vacancy varied from fully fluorinated (4F) to hydroxy-fluorinated (3F + 1OH, 2F + 2OH, 1F + 3OH) to fully hydroxylated (4OH). The calculated intercalation energies, as a function of *X* are shown in **Figure 5b**. For a purely-fluorine-compensated vacant site, the intercalation energy of Al^{3+} is -3.1 eV. Partial or complete replacement of F with OH neighbouring the vacancy sites reduces the absolute value of the intercalation energy to ~-2.5 eV, indicating that hydroxy-fluorinated environments are generally less accommodating of Al^{3+}. According to ^{19}F NMR, only a small proportion of single-vacant sites are capable of accommodating Al^{3+} ions. Our calculations indicate that these are likely to be fluorine-rich vacancy environments, which are statistically less likely than hydroxylated or mixed-hydroxy-fluorinated environments.[47] This suggests that the poor ability of Al^{3+} to be inserted in single vacant site is primary due to the local environment of the vacancy.

To better understand how anionic environment affects the intercalation properties of neighbouring interstitial sites, we performed additional DFT calculations with Al atoms occupying interstitial sites adjacent to a single vacancy. For each anion combination, we plotted all inequivalent vacancy-adjacent positions in **Figure 5b** as grey points. The intercalation energies show a broad spread, due to the variation in the local geometry (both the local anion configuration, and the interstitial position relative to the vacancy site). Furthermore, in all cases some of these intercalation energies are more favourable than for insertion at an isolated interstitial site in pristine anatase TiO_2. Analysis of the Al–(O/F) coordination modes from our calculations revealed that Al^{3+} located in Ti-vacancy sites strictly

adopts 6-fold coordination, while Al^{3+} inserted into interstitial sites is under-coordinated, specifically being 5-fold coordinated, further explaining the ^{27}Al NMR data. The occurrence of 4-fold coordination mode was, however, not captured by DFT-calculations. We postulate that this might be due to the fact that electrochemical insertion is performed under non-equilibrium conditions. Time-dependent ^{27}Al NMR experiments, indeed, revealed that these "4-coordinate" insertion sites are unstable with their proportion decreasing upon aging. Another potential contributing factor is the possibility of structural heterogeneity within our experimental samples, or additional geometric distortions due to defect–defect interactions at high (F/OH)-doping levels, which may potentially lead to off-centre Al^{3+} forming a 4-fold coordination mode, *i.e.*, 4+2.

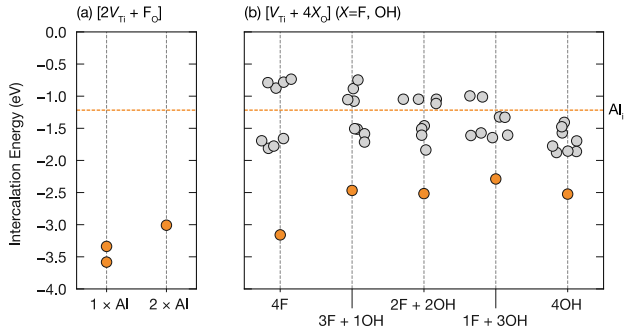

Figure 5. Intercalation energies of Al^{3+}. (a) Average intercalation energies for 1 Al and 2 Al into a double-vacancy of the $Ti_{126}\square_2O_{248}F_8$ supercell. (b) Intercalation energies for Al into a single-vacancy of the $Ti_{127}\square_1O_{252}X_4$ supercell for X = {F, OH}. The horizontal dashed line shows the intercalation energy for Al^{3+} in stoichiometric anatase TiO_2 at an interstitial site. *Source*: source data, figure files, and plotting scripts are available under the CC-BY-4.0 license as part of reference[48].

Conclusion

To summarize, we investigated the insertion mechanism of Al^{3+} into defective anatase. About ~0.10 Al^{3+} per formula unit can be electrochemically inserted in the structure via solid-solution behaviour with negligible volume changes. Pair distribution function analysis revealed that Al^{3+} induces local distortions, that were accurately captured by DFT-calculations. Such local distortions affect the insertion properties of neighbouring pairs of Ti vacancies, providing a possible explanation for the limited number of Al^{3+} that can be reversibly inserted. The intercalation mechanism is found to involve a number of different types of host sites; specifically, native interstitial sites, single-Ti-vacancy sites, and double-Ti-vacancy sites. Al^{3+} adopts a 6-fold coordination mode in Ti-vacancy sites, while Al^{3+} is under-coordinated when occupying interstitial sites, as shown by ^{27}Al NMR and DFT-calculations. Within the double-vacancy, inserting two Al^{3+} is less favourable than inserting one Al^{3+}. This corresponds to about 40% of the total number of vacancies, which translates to 0.045 vacancy per formula unit that readily accommodate Al^{3+} ions. Moreover, a limited number of fully-fluorinated single-vacancy sites are predicted to be electrochemically active, highlighting the key role of the local anion environment. Local anion configurations also affect the insertion properties of interstitial sites, which may also contribute to the insertion mechanism. Overall, this work highlights specific structural features induced by the intercalation electrochemistry of tri-valent cation which should be considered when designing new electrode materials for polyvalent batteries.

Acknowledgements

The research leading to these results has received funding from the French National Research Agency under Idex@Sorbonne University for the Future Investments program (No. ANR-11-IDEX-0004-02) and by the German Federal Ministry of Education and Research (BMBF) through funding by the "Sino German TU9 network for electromobility" under the grant reference number 16N11929. Financial support from the IR-RMN-THC Fr3050 CNRS for conducting the research is gratefully acknowledged. B. J. M. acknowledges support from the Royal Society (UF130329 & URF\R\191006). This work made use of the ARCHER UK National Supercomputing Service (http://www.archer.ac.uk), via the membership of the UK's HPC Materials Chemistry Consortium, which is funded by EPSRC (EP/L000202). The work done at the Advanced Photon Source, an Office of Science User Facility operated for the U.S. Department of Energy (DOE) Office of Science by Argonne National Laboratory, was supported by the U.S. DOE under Contract No. DE-AC02-06CH11357. D.D, C.L, M.B wish to thank the French fluorine network for continuous support.

Keywords: Polyvalent ion batteries • ^{27}Al and ^{19}F solid state NMR • vacancy • local distortion • insertion mechanism

[1] J.-M. Tarascon, *Nat Chem* **2010**, *2*, 510–510.
[2] C. P. Grey, J. M. Tarascon, *Nat Mater* **2017**, *16*, 45–56.
[3] K. Kubota, M. Dahbi, T. Hosaka, S. Kumakura, S. Komaba, *The Chemical Record* **2018**, *18*, 459–479.
[4] P. Canepa, G. Sai Gautam, D. C. Hannah, R. Malik, M. Liu, K. G. Gallagher, K. A. Persson, G. Ceder, *Chem. Rev.* **2017**, *117*, 4287–4341.
[5] H. Yang, H. Li, J. Li, Z. Sun, K. He, H.-M. Cheng, F. Li, *Angewandte Chemie International Edition* **2019**, *58*, 11978–11996.
[6] T. Leisegang, F. Meutzner, M. Zschornak, W. Münchgesang, R. Schmid, T. Nestler, R. A. Eremin, A. A. Kabanov, V. A. Blatov, D. C. Meyer, *Front. Chem.* **2019**, *7*, DOI 10.3389/fchem.2019.00268.
[7] G. A. Elia, K. Marquardt, K. Hoeppner, S. Fantini, R. Lin, E. Knipping, W. Peters, J.-F. Drillet, S. Passerini, R. Hahn, *Adv. Mater.* **2016**, *28*, 7564–7579.
[8] J. Shi, J. Zhang, J. Guo, *ACS Energy Lett.* **2019**, *4*, 2124–2129.
[9] M.-C. Lin, M. Gong, B. Lu, Y. Wu, D.-Y. Wang, M. Guan, M. Angell, C. Chen, J. Yang, B.-J. Hwang, H. Dai, *Nature* **2015**, *520*, 324–328.
[10] M. Walter, K. V. Kravchyk, C. Böfer, R. Widmer, M. V. Kovalenko, *Advanced Materials* **2018**, *30*, 1705644.
[11] D. B. Le, S. Passerini, F. Coustier, J. Guo, T. Soderstrom, B. B. Owens, W. H. Smyrl, *Chem. Mater.* **1998**, *10*, 682–684.
[12] W. Wang, B. Jiang, W. Xiong, H. Sun, Z. Lin, L. Hu, J. Tu, J. Hou, H. Zhu, S. Jiao, *Scientific Reports* **2013**, *3*, srep03383.
[13] B. Lee, H. R. Lee, T. Yim, J. H. Kim, J. G. Lee, K. Y. Chung, B. W. Cho, S. H. Oh, *J. Electrochem. Soc.* **2016**, *163*, A1070–A1076.
[14] L. Geng, J. P. Scheifers, C. Fu, J. Zhang, B. P. T. Fokwa, J. Guo, *ACS Appl. Mater. Interfaces* **2017**, *9*, 21251–21257.
[15] H. Wang, Y. Bai, S. Chen, X. Luo, C. Wu, F. Wu, J. Lu, K. Amine, *ACS Appl. Mater. Interfaces* **2015**, *7*, 80–84.
[16] A. VahidMohammadi, A. Hadjikhani, S. Shahbazmohamadi, M. Beidaghi, *ACS Nano* **2017**, *11*, 11135–11144.
[17] L. Geng, J. P. Scheifers, J. Zhang, K. N. Bozhilov, B. P. T. Fokwa, J. Guo, *Chem. Mater.* **2018**, *30*, 8420–8425.
[18] S. K. Das, T. Palaniselvam, P. Adelhelm, *Solid State Ionics* **2019**, *340*, 115017.
[19] S. Wang, K. V. Kravchyk, S. Pigeot-Rémy, W. Tang, F. Krumeich, M. Wörle, M. I. Bodnarchuk, S. Cassaignon, O. Durupthy, S. Zhao, C. Sanchez, M. V. Kovalenko, *ACS Appl. Nano Mater.* **2019**, *2*, 6428–6435.
[20] M. Wagemaker, W. J. H. Borghols, F. M. Mulder, *J. Am. Chem. Soc.* **2007**, *129*, 4323–4327.

[21] L. Wu, D. Buchholz, D. Bresser, L. Gomes Chagas, S. Passerini, *Journal of Power Sources* **2014**, *251*, 379–385.
[22] T. Koketsu, J. Ma, B. J. Morgan, M. Body, C. Legein, W. Dachraoui, M. Giannini, A. Demortière, M. Salanne, F. Dardoize, H. Groult, O. J. Borkiewicz, K. W. Chapman, P. Strasser, D. Dambournet, *Nature Materials* **2017**, *16*, 1142.
[23] T. Koketsu, J. Ma, B. J. Morgan, M. Body, C. Legein, W. Dachraoui, M. Giannini, A. Demortière, M. Salanne, F. Dardoize, H. Groult, O. J. Borkiewicz, K. W. Chapman, P. Strasser, D. Dambournet, *Nat. Mater.* **2017**, *16*, 1142–1148.
[24] W. Li, D. Corradini, M. Body, C. Legein, M. Salanne, J. Ma, K. W. Chapman, P. J. Chupas, A.-L. Rollet, C. Julien, K. Zhagib, M. Duttine, A. Demourgues, H. Groult, D. Dambournet, *Chem. Mater.* **2015**, *27*, 5014–5019.
[25] D. A. Keen, *J Appl Cryst, J Appl Crystallogr* **2001**, *34*, 172–177.
[26] T. Egami, S. J. L. Billinge, *Underneath the Bragg Peaks: Structural Analysis of Complex Materials*, Elsevier, **2003**.
[27] J. Jiang, H. Li, J. Huang, K. Li, J. Zeng, Y. Yang, J. Li, Y. Wang, J. Wang, J. Zhao, *ACS Appl. Mater. Interfaces* **2017**, *9*, 28486–28494.
[28] P. Daniel, A. Bulou, M. Rousseau, J. Nouet, J. L. Fourquet, M. Leblanc, R. Burriel, *J. Phys.: Condens. Matter* **1990**, *2*, 5663–5677.
[29] A. Le Bail, C. Jacoboni, M. Leblanc, R. De Pape, H. Duroy, J. L. Fourquet, *Journal of Solid State Chemistry* **1988**, *77*, 96–101.
[30] D. Dambournet, A. Demourgues, C. Martineau, S. Pechev, J. Lhoste, J. Majimel, A. Vimont, J.-C. Lavalley, C. Legein, J.-Y. Buzaré, F. Fayon, A. Tressaud, *Chem. Mater.* **2008**, *20*, 1459–1469.
[31] D. Dambournet, A. Demourgues, C. Martineau, E. Durand, J. Majimel, A. Vimont, H. Leclerc, J.-C. Lavalley, M. Daturi, C. Legein, J.-Y. Buzaré, F. Fayon, A. Tressaud, *J. Mater. Chem.* **2008**, *18*, 2483.
[32] B. Ollivier, R. Retoux, P. Lacorre, D. Massiot, G. Férey, *Journal of Materials Chemistry* **1997**, *7*, 1049–1056.
[33] C. Ferrara, V. Dall'Asta, V. Berbenni, E. Quartarone, P. Mustarelli, *The Journal of Physical Chemistry C* **2017**, *121*, 26607–26614.
[34] J. W. Akitt, *Progress in Nuclear Magnetic Resonance Spectroscopy* **1989**, *21*, 1–149.
[35] D. Massiot, F. Fayon, M. Capron, I. King, S. Le Calvé, B. Alonso, J.-O. Durand, B. Bujoli, Z. Gan, G. Hoatson, *Magnetic Resonance in Chemistry* **2002**, *40*, 70–76.
[36] W. Zhang, M. Sun, R. Prins, *J. Phys. Chem. B* **2002**, *106*, 11805–11809.
[37] P. J. Chupas, C. P. Grey, *Journal of Catalysis* **2004**, *224*, 69–79.
[38] J. Ma, W. Li, B. J. Morgan, J. Światowska, R. Baddour-Hadjean, M. Body, C. Legein, O. J. Borkiewicz, S. Leclerc, H. Groult, F. Lantelme, C. Laberty-Robert, D. Dambournet, *Chem. Mater.* **2018**, *30*, 3078–3089.
[39] S. K. Lee, S. B. Lee, S. Y. Park, Y. S. Yi, C. W. Ahn, *Phys. Rev. Lett.* **2009**, *103*, 095501.
[40] S. K. Lee, S. Y. Park, Y. S. Yi, J. Moon, *J. Phys. Chem. C* **2010**, *114*, 13890–13894.
[41] V. Sarou-Kanian, A. N. Gleizes, P. Florian, D. Samélor, D. Massiot, C. Vahlas, *The Journal of Physical Chemistry C* **2013**, *117*, 21965–21971.
[42] R. Hoppe, St. Becker, *Zeitschrift für anorganische und allgemeine Chemie* **1989**, *568*, 126–135.
[43] P. Daniel, A. Bulou, M. Rousseau, J. Nouet, M. Leblanc, *Physical Review B* **1990**, *42*, 10545–10552.
[44] N. Herron, D. L. Thorn, R. L. Harlow, G. A. Jones, J. B. Parise, J. A. Fernandez-Baca, T. Vogt, *Chemistry of Materials* **1995**, *7*, 75–83.
[45] A. Sadoc, M. Biswal, M. Body, C. Legein, F. Boucher, D. Massiot, F. Fayon, *Solid State Nuclear Magnetic Resonance* **2014**, *59–60*, 1–7.
[46] E. Nimerovsky, R. Gupta, J. Yehl, M. Li, T. Polenova, A. Goldbourt, *Journal of Magnetic Resonance* **2014**, *244*, 107–113.
[47] J. Ma, T. Koketsu, B. J. Morgan, C. Legein, M. Body, P. Strasser, D. Dambournet, *Chem. Commun.* **2018**, *54*, 10080–10083.
[48] B. Morgan, Computational Supporting Dataset: Atomic Insights into Aluminium-Ion Insertion in Defective Hydroxyfluorinated Anatase for Batteries.Bath: University of Bath Research Data Archive. doi.org/10.15125/BATH-00815.

Entry for the Table of Contents

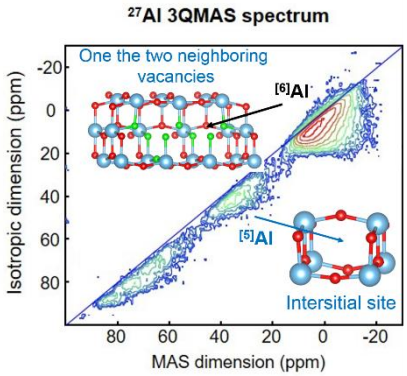

The intercalation mechanism of high-charge Al^{3+} ions in cationic-defective anatase was elucidated providing fundamental insights into key factors that impact the total number of inserted ions. Such factors are the nature of insertion sites, their surrounding anions and the polarizing power of Al^{3+}.